Carlson, K.D., Melendez, A.J., and Beckermann, C., "Modeling of Reoxidation Inclusion Formation in Steel Sand Casting," in Proceedings of the 63rd SFSA Technical and Operating Conference, Paper No. 5.6, Steel Founders' Society of America, Chicago, IL, 2009.

Modeling of Reoxidation Inclusion Formation in Steel Sand Casting

K.D. Carlson, A.J. Melendez and C. Beckermann

Mechanical and Industrial Engineering Dep't, University of Iowa, Iowa City, Iowa 52242

Abstract

A model is developed that predicts the motion and growth of oxide inclusions during pouring, as well as their final locations on the surface of steel sand castings. Inclusions originate on the melt free surface, and their subsequent growth is controlled by oxygen transfer from the atmosphere. Inclusion motion is modeled in a Lagrangian sense, taking into account drag and buoyancy forces. The inclusion model is implemented in a general-purpose casting simulation code. The model is validated by comparing the simulation results to measurements made on production steel sand castings. Good overall agreement is obtained. In addition, parametric studies are performed to investigate the sensitivity of the predictions to various model parameters.

1. Introduction

The removal of oxide inclusions from the surface of steel sand castings and the subsequent repair of those castings are expensive and time consuming. Inclusions that remain in the casting adversely affect machining and mechanical performance, and may cause the casting to be rejected for failing to meet the requirements specified by the customer regarding allowable inclusion severity. Reoxidation inclusions, which form when deoxidized steel comes into contact with oxygen during mold filling, make up a substantial portion of the inclusions found in steel castings. It has been estimated that 83% of the macro-inclusions found in carbon and low-alloy (C&LA) steel castings are reoxidation inclusions.[1] The primary source of oxygen in reoxidation inclusion formation is air, which contacts the metal stream during pouring as well as the metal free surface in the mold cavity during filling.

The objective of the present work is to develop a numerical model that simulates the motion and growth of reoxidation inclusions during the pouring of C&LA steel castings. The oxide mixture that forms during the pouring of C&LA steel is partially liquid,[2] as opposed to the solid oxide films or particles that form during casting of high-alloy steel or light metals. Thus, the

present model considers inclusions to be individual particles, rather than part of a film. This inclusion model, which is developed within a general-purpose casting simulation package, predicts the distribution of reoxidation inclusions on the surface of C&LA steel sand castings at the end of filling. This information can be used to help determine whether a given rigging design will lead to inclusion problems before production, and can indicate what effect rigging modifications have on the inclusion distribution.

The inclusion model is presented in the next section. Following this, three different production casting inclusion case studies are described, including a description of the methodology utilized to measure inclusions on the surface of these castings. Next, simulated inclusion results are presented for these case studies, and the simulated results are compared with the measured results. Finally, parametric studies are performed to investigate the sensitivity of the simulation results to various model parameters.

2. Model Description

The inclusion calculations described in this section are performed as part of a standard casting filling simulation. The filling simulation calculates the velocity and free surface geometry of the melt as a function of time during mold filling. The inclusion model assumes that the reoxidation inclusions are spherical, characterized by their diameter, d_{inc}, as depicted in Fig. 1. The inclusions form and grow only on the melt free surface, but they are transported throughout the melt volume by the flow during filling. The present model tracks the inclusions in a Lagrangian sense. This section describes the equations employed within the inclusion model. Additional detail regarding this model can be found in references 2 and 3.

2.1 Inclusion Generation

Inclusions are generated during a filling simulation by searching the free surface at the beginning of each time step, and if a localized region of the free surface does not contain any inclusions, then tiny inclusions are added over the region, with a spacing of L_{sp}. The initial size of these introduced inclusions, d_{gen}, is taken as a very small value, such that the initial inclusion volume added by placing these inclusions on the free surface is negligibly small. During each time step in a filling simulation, new free surface area is created; also, some inclusions on existing regions of the free surface may be swept away from the surface (into the bulk of the

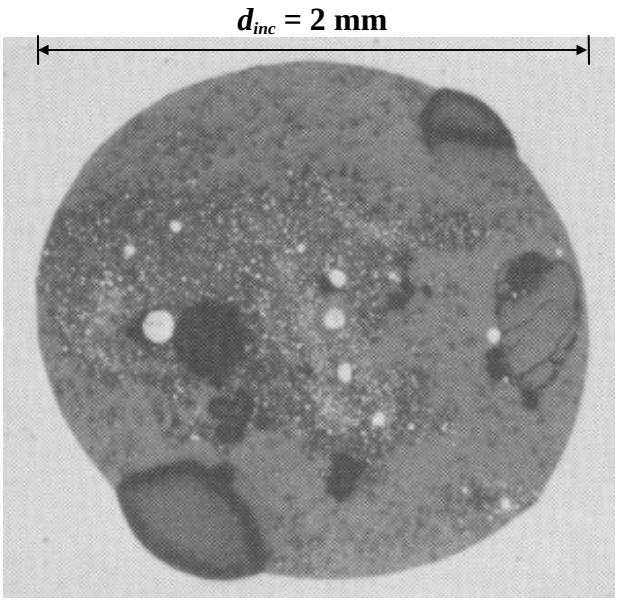

Figure 1. Image of a typical reoxidation inclusion.

melt) by the local flow pattern. Both of these situations create regions of the free surface lacking inclusions, where new inclusions will be generated. The total number of inclusions generated during a filling simulation, therefore, is a direct function of the free surface evolution and the tendency of the flow to draw inclusions away from the free surface, as well as the inclusion generation spacing, L_{sp}.

2.2 Inclusion Growth

The growth of reoxidation inclusions occurs due to the mass transfer of oxygen through the air to the melt-air interface. When an inclusion is on the melt free surface, it grows according to:[2]

$$\partial V_{inc} / \partial t = A_{FS,inc} \beta \tag{1}$$

where V_{inc} is the inclusion volume; t is time; β is a growth coefficient; and $A_{FS,inc}$ represents the area of the melt free surface that contributes oxide to the growing inclusion. This area is determined by apportioning the total melt free surface area among all inclusions present on the surface, weighted by each inclusion's volume. The growth coefficient in equation (1) is modeled as:[2]

$$\beta = \frac{r_{inc} M_{inc}}{\rho_{inc}} \frac{D_{O_2}}{\delta_{O_2}} \frac{p_{O_2}}{\overline{R} T} \tag{2}$$

where r_{inc} is the ratio of the number of moles of inclusions to the number of moles of diatomic oxygen (O_2) consumed; M_{inc} is the effective molecular weight of the inclusions; ρ_{inc} is the effective inclusion density; D_{O_2} is the mass diffusivity of O_2 gas in the atmosphere; p_{O_2} is the partial pressure of O_2 gas in the atmosphere; T is the absolute air temperature at the melt-air interface; $\overline{R}$ is the universal gas constant; and δ_{O_2} is the thickness of the oxygen boundary layer at the melt free surface. Values for the various properties and constants used in the present calculations are listed in Table 1. Material property values given in Table 1 were evaluated at the pouring temperature. The carbon monoxide gas that forms amid oxidation of C&LA steels during pouring is not taken into account.[2] It is seen from equation (2) that the growth coefficient is proportional to the partial pressure of molecular oxygen, and is inversely proportional to the boundary layer thickness.

Table 1. Parameters and constants used to simulate inclusions.[2]

Quantity	**Value**
Inclusion moles per mole of molecular oxygen (r_{inc})	0.42
Effective molecular weight of inclusions (M_{inc})	149 g/mol
Effective inclusion density (ρ_{inc})	3.23 g/cm^3
Diffusivity of oxygen in air (D_{O_2})	4.56 cm^2/s
Partial pressure of oxygen in air (p_{O_2})	21287.25 Pa
Universal gas constant $(\overline{R})$	8.314×10^6 Pa-cm^3/mol-K
Kinematic viscosity of air (ν_a)	3.53 cm^2/s
Density of liquid steel (ρ_l)	6.95 g/cm^3
Kinematic viscosity of liquid steel (ν_l)	0.00648 cm^2/s
Gravitational acceleration $(\lvert \boldsymbol{g} \rvert)$	981 cm/s^2
Generated inclusion diameter (d_{gen})	10 μm
Characteristic length (L_c)	30 mm

In the present work, the oxygen boundary layer thickness, δ_{O_2}, is determined using the following correlation:

$$\delta_{O_2} = L_c \Big/ \left\{ 2 + 0.6\,\mathrm{Re}^{1/2}\,\mathrm{Sc}^{1/3} \right\} \tag{3}$$

where L_c is a characteristic length of the melt free surface; Re is the Reynolds number, $\mathrm{Re} = |\boldsymbol{u_l} - \boldsymbol{u_a}| L_c / \nu_a$, which is defined in terms of the magnitude of the relative velocity between the liquid metal free surface and the air; Sc is the Schmidt number, $\mathrm{Sc} = \nu_a / D_{O_2}$; and ν_a is the kinematic viscosity of the air. It is assumed that the air velocity is negligible, so the Reynolds number simplifies to $\mathrm{Re} = |\boldsymbol{u_l}| L_c / \nu_a$. Equation (3) is the Ranz-Marshall correlation,[4] which models heat and mass transfer for droplets of diameter L_c. Although the metal free surface is generally not made up of droplets, this correlation is used to obtain an estimate of the oxygen boundary layer thickness. In the present context, L_c can be thought of as a characteristic free surface length, such as an effective diameter or length of a portion of the free surface. As a first approximation, L_c is taken as a constant in the present model. Since detailed pouring characteristics such as splashing and (surface) turbulence, which greatly influence the free surface and thus inclusion development, are not accurately resolved by general-purpose casting simulation packages, it makes little sense to implement a more complex model for the oxygen transport at the surface.

As indicated by equations (1) through (3), the inclusion volume increase at each time step is calculated as a function of the free surface area apportioned to each inclusion, $A_{FS,inc}$, the local melt surface velocity, $\boldsymbol{u}_l$, and the characteristic free surface length, L_c. To better understand the effects of the melt velocity and characteristic length on the resulting inclusion volume, it is useful to apply the present growth model to estimate the total reoxidation inclusion volume that forms during the pouring of a steel casting. Summing over all inclusions and assuming, for this estimate only, that the growth coefficient β is constant with time and the same for all inclusions, equation (1) can be integrated over the pouring time and divided by the total steel volume, V_s, to yield the total inclusion volume fraction in a casting:

$$g_{inc} = \frac{V_{inc}}{V_s} = \beta \left(\frac{1}{V_s} \int_0^{t_{pour}} A_{FS}\, dt \right) \tag{4}$$

In order to obtain a rough estimate of the value in the parentheses in this equation, filling

simulations were performed for three different production castings. For all three castings, the value in the parentheses was approximately 100 s/m. Using this value, and using equations (2) and (3) to calculate β, the inclusion volume fraction was computed from equation (4) for a range of characteristic free surface lengths and melt surface velocities. The result of this parametric study is shown in Fig. 2. The four curves in this figure correspond to a reasonable range of melt surface velocities. Note that for small characteristic lengths, these equations predict very large inclusion volume fractions. However, for characteristic lengths from about 20 to 50 mm, the inclusion volume fractions are reasonable [several hundred parts per million (ppm), or less than one in^3/ft^3] over the range of velocities shown. For the present study, a constant characteristic length of $L_c = 30$ mm was chosen. For a free surface velocity of 1 m/s, this value gives an inclusion volume fraction of approximately 300 ppm, or 0.5 in^3/ft^3. Fig. 3 shows the relationship between the inclusion volume fraction and the ratio of ambient air consumption (needed to supply the oxygen) to total steel volume. For an inclusion volume fraction of 300 ppm

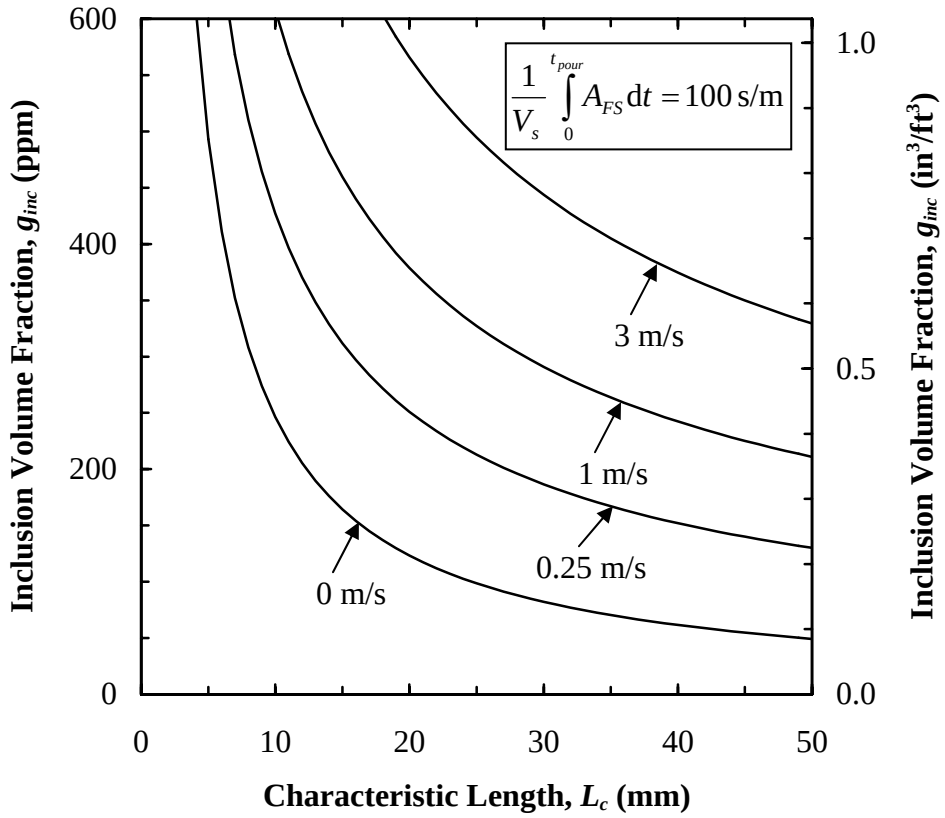

Figure 2. Variation of inclusion volume fraction with characteristic free surface length and melt surface velocity.

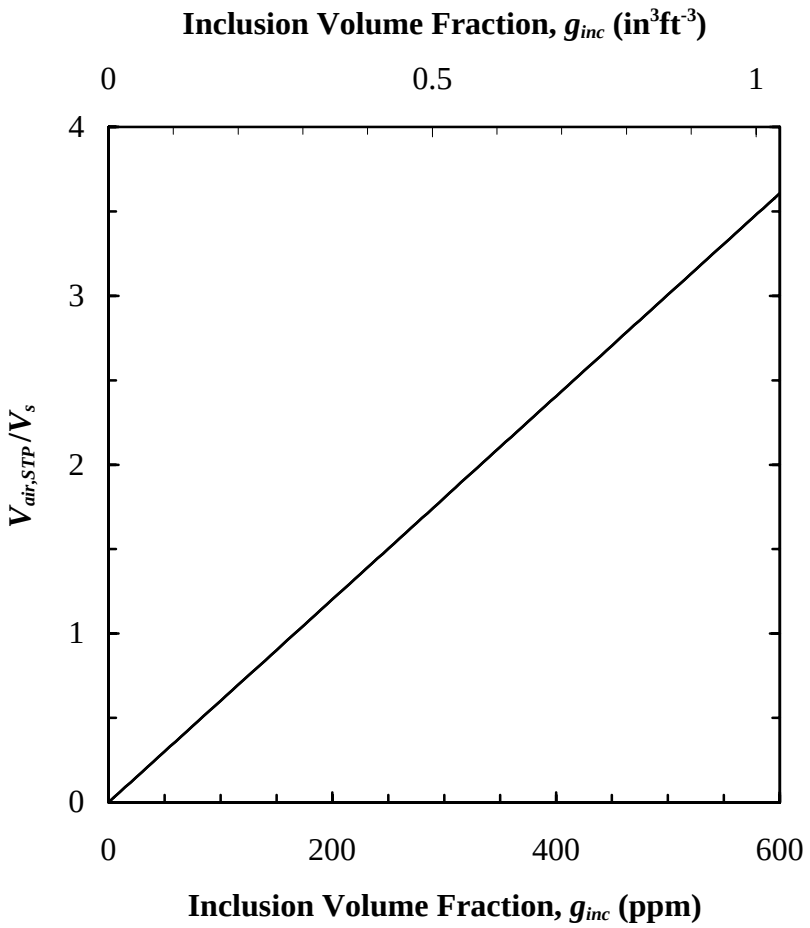

Figure 3. Variation of ambient air consumption with inclusion volume fraction.

(0.5 in^3/ft^3), the ambient air volume consumed is approximately 1.8 times the steel volume, which seems reasonable: $1.0V_s$ from the air initially in the mold, plus $0.8V_s$ from air entrained during filling. This indicates that the choice of $L_c = 30$ mm should produce a reasonable volume of inclusions.

2.3 Inclusion Motion

The final inclusion locations are determined by tracking the motion of each inclusion from its initial generation on the free surface until the end of filling. This is accomplished by solving, for each inclusion at each time step, the following equation of motion:

$$\rho_{inc}\frac{d\boldsymbol{u}_{\boldsymbol{inc}}}{dt}=\underbrace{\frac{18\rho_l\nu_l}{d_{inc}^2}\left(\boldsymbol{u}_{\boldsymbol{l}}-\boldsymbol{u}_{\boldsymbol{inc}}\right)\left(1+0.15\,\mathrm{Re}_{inc}^{0.687}\right)}_{\text{drag}}+\underbrace{\left(\rho_{inc}-\rho_l\right)\boldsymbol{g}}_{\text{bouyancy}} \tag{5}$$

where the subscripts indicate whether the quantity is associated with the inclusion ('*inc*') or with the liquid metal ('*l*'); and $\boldsymbol{g}$ is the gravity vector. In equation (5), Re_{inc} is the inclusion Reynolds number, $\mathrm{Re}_{inc}=\left|\boldsymbol{u}_{\boldsymbol{l}}-\boldsymbol{u}_{\boldsymbol{inc}}\right|d_{inc}/\nu_l$, which is defined in terms of the magnitude of the relative velocity between the melt and the inclusion. The melt velocity, $\boldsymbol{u}_{\boldsymbol{l}}$, available from the filling simulation, is interpolated to the location of the inclusion. Note that equation (5) accounts for both buoyancy and drag forces. Once the velocity of each inclusion has been determined using equation (5), this information is used to update the location of each inclusion according to $d\boldsymbol{x}_{inc}/dt=\boldsymbol{u}_{inc}$, where $\boldsymbol{x}_{inc}$ is the inclusion's position vector.

If an inclusion comes into contact with a mold wall, as shown schematically in Fig. 4, the inclusion's velocity along the wall is determined using the following friction law-type equation:

$$\boldsymbol{u}_{inc}^{t}\Big|_{wall}=\lambda_{inc}\frac{\partial\boldsymbol{u}_{inc}^{t}}{\partial n} \tag{6}$$

where n is the direction normal to the mold wall; the superscript t indicates that the velocity is tangential to the mold wall; and λ_{inc} is a slip coefficient, which has units of length. Note that when equation (6) is discretized, the inclusion velocity at a distance Δn from the wall, $\boldsymbol{u}_{inc}^{t}\big|_{\Delta n}$, is

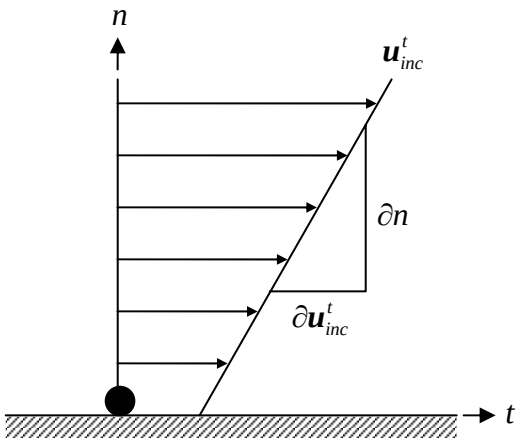

Figure 4. Schematic of slip condition at mold/metal interface.

approximated by the melt velocity at that location, $\boldsymbol{u}_l^t\big|_{\Delta n}$. Equation (6) indicates that the inclusion velocity at the wall is directly proportional to the inclusion velocity gradient in the region; increasing the gradient increases the shear force on the inclusion, which increases the inclusion velocity at the wall. Note that when $\lambda_{inc} = 0$, equation (6) reduces to a no slip condition at the wall. Conversely, as $\lambda_{inc} \to \infty$, it is required that $\partial \boldsymbol{u}_{inc}^t / \partial n \to 0$ in order to keep $\boldsymbol{u}_{inc}^t\big|_{wall}$ finite; this condition implies a uniform velocity profile (i.e., plug flow), and represents a full slip condition at the wall. Values of λ_{inc} between zero and infinity imply a partial slip condition. In the present study, λ_{inc} is considered an adjustable constant. The value of this parameter is determined via comparison with measured results.

2.4 Inclusion Agglomeration

For typical production castings, simulating every inclusion in a casting quickly becomes computationally overwhelming. Typical aluminum-killed low alloy steel contains about 10^8 inclusions per kilogram of steel,[5] which gives an inclusion number density on the order of 10^{12} m^{-3}. With the present model, inclusion tracking is reasonable up to about 10^6 to 10^7 inclusions; beyond this, computational speed and storage become problematic issues. However, the vast majority of the 10^{12} m^{-3} inclusions are tiny. In continuous casting of steel, it has been found that only about 10^7 m^{-3} inclusions are larger than 80 microns in diameter, and the number larger than 200 microns is on the order of 10^4 m^{-3}.[5] In steel sand casting, the tiny (less than 80 microns) inclusions are not a concern in terms of surface quality. Although large in number, tiny inclusions make up a small percentage of the total inclusion volume. Furthermore, they lack buoyancy due to their small size, and are thus distributed relatively evenly throughout the casting. It is only the larger inclusions that are of interest here. The present model attempts to track the larger inclusions through the use of agglomeration, which is controlled through specification of an agglomeration length. During each simulation time step, the agglomeration algorithm considers each inclusion, and finds all other inclusions whose centers are within the agglomeration length from the center of the inclusion under consideration. All inclusions within this distance are combined into a single, agglomerated inclusion, preserving overall inclusion volume and momentum. This model favors larger inclusions, neglecting the immense number of

small inclusions by absorbing them into larger ones. It is emphasized that the actual physics of inclusion agglomeration are not considered in the present model. The primary goal of the agglomeration model is to make inclusion simulations computationally feasible by limiting the number of inclusions to a manageable quantity, while preserving the total oxide volume and predicting reasonable sizes and velocities for the larger inclusions. Note that in the present model, it would be senseless to have an agglomeration length larger than the inclusion generation spacing, L_{sp}; inclusions would be generated and then immediately agglomerated together in the same time step. Therefore, both the generation spacing and the agglomeration length are taken to be the same value, L_{sp}. The agglomeration length is considered an adjustable constant in this study.

3. Production Casting Inclusion Measurements

The present study includes inclusion measurements for three plain carbon steel production parts: a bracket, a spindle, and a lever arm. The bracket, shown schematically with its rigging in Fig. 5, weighs 330 kg (726 lb), and is cast from AISI 1522 steel in a phenolic urethane no bake (PUNB) mold. The spindle, shown in Fig. 6, weighs 2126 kg (4677 lb), and the lever arm, shown in Fig. 7, weighs 575 kg (1265 lb). Both the spindle and the lever arm are cast from WCB steel in a phenolic urethane cold box (PUCB) mold. All castings are poured from a bottom-pour ladle.

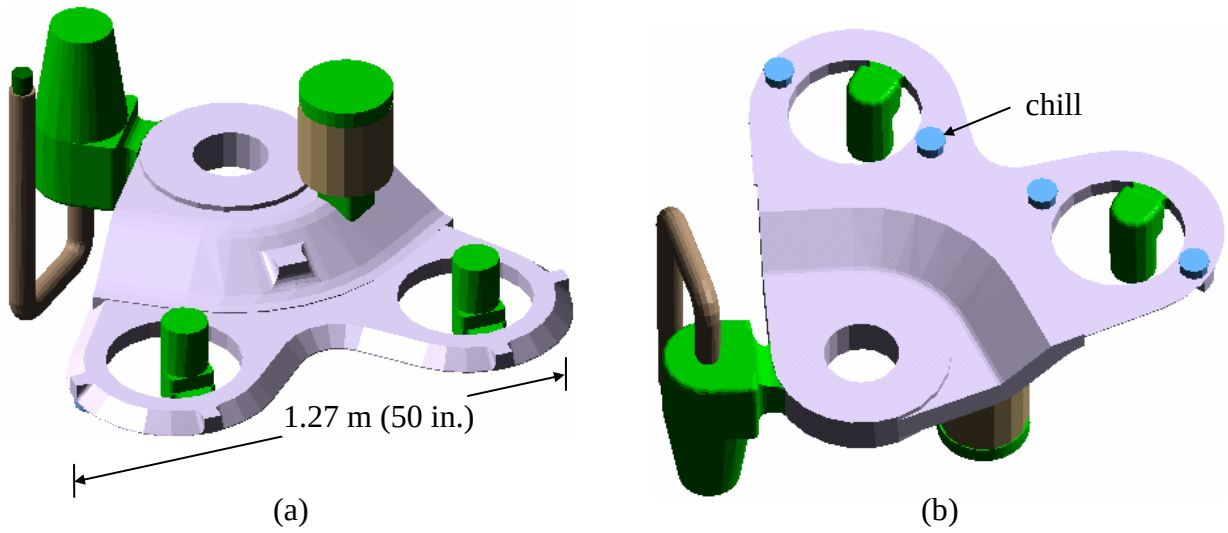

Figure 5. Two schematic views of rigging for bracket castings, showing risers and gating.

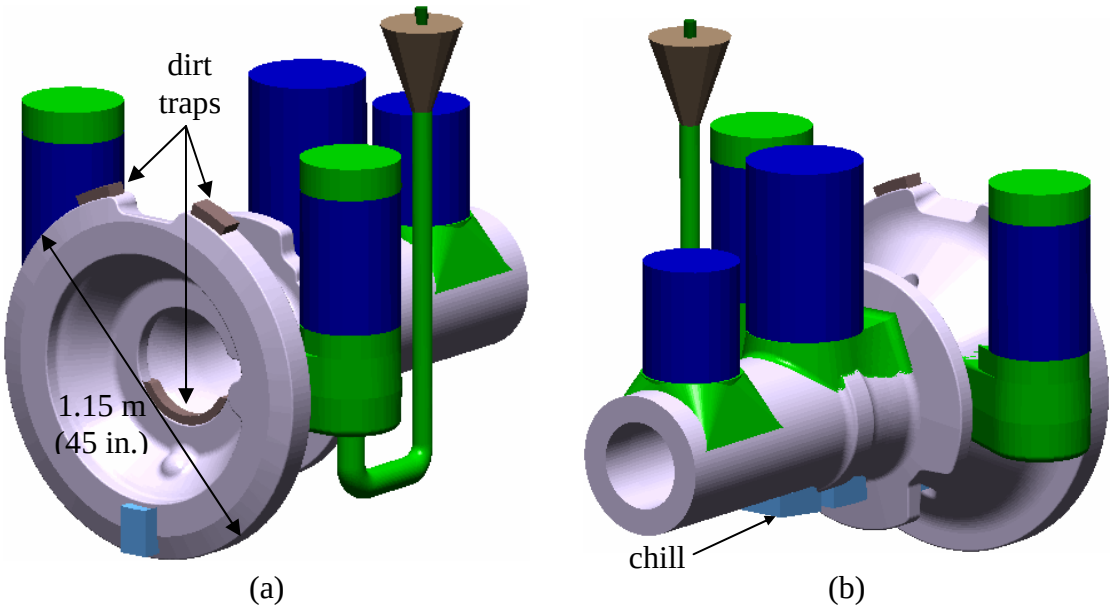

Figure 6. Two schematic views of rigging for spindle castings, showing risers and gating.

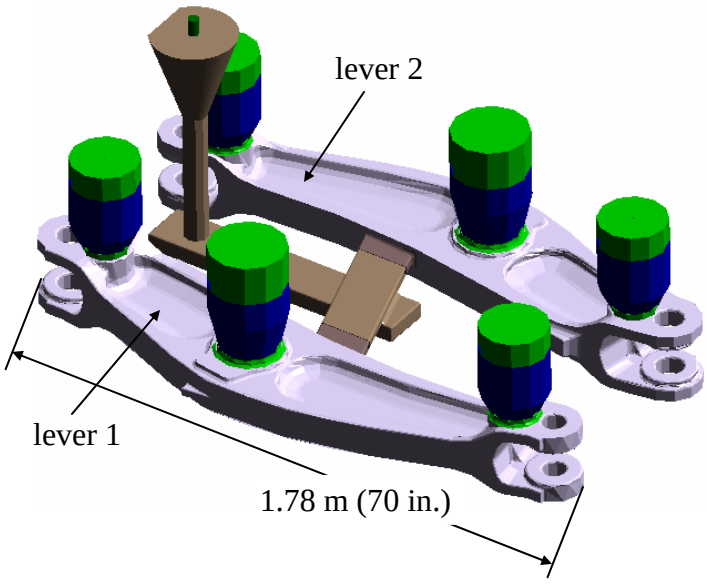

Figure 7. Schematic of rigging for lever arm castings, showing risers and gating.

For each part, inclusions were measured at the steel foundry on many individual castings: 28 brackets, 30 spindles, and 29 lever arms. Inclusion measurements for each individual casting were recorded by noting the position of all inclusions on a casting, and then mapping those inclusion locations onto a solid model of the casting, assigning a value of one to inclusions and a value of zero to areas without inclusions. An example of such a digitized inclusion concentration

result is shown for one lever arm casting in Fig. 8a, where the dark circles on the lever arm surface denote inclusions. For the lever arm and the spindle, noted inclusions were mapped onto the solid model as circles, having a diameter equal to the number of "inches of dirt" measured for each inclusion. For the bracket, on the other hand, a 2.54 cm (one inch) square grid was overlaid onto the entire casting surface, and any grid square containing one or more inclusions was assigned a value of one. For both measurement techniques, the minimum resolution was 2.54 cm (one inch). For each part (bracket, spindle and lever arm), the inclusion concentration results for each individual casting of that part (such as the one shown in Fig. 8a) were then superimposed, summing the digitized inclusion values at each location on the casting surface and then dividing by the number of castings. This provides the probability (from 0 to 1) that an inclusion is present at a given point on the casting surface of each part. The final inclusion probability distribution is

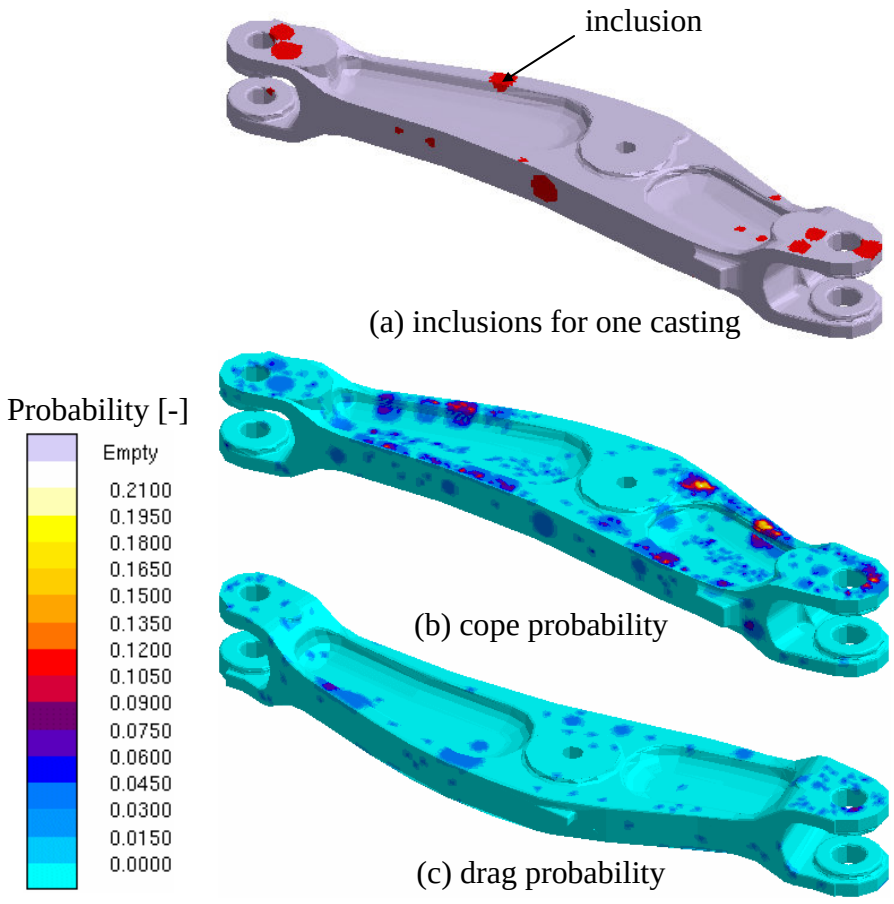

Figure 8. (a) Digitized inclusion concentration measurements for one lever arm casting, along with two views [(b) and (c)] of the final measured inclusion probability distribution for the lever arm.

shown for two views of the lever arm in Figs. 8b and 8c. Final inclusion probability distributions for the bracket and the spindle are given in Figs. 9 and 10, respectively. Note that for all three parts shown in Figs. 8 – 10, the higher values of inclusion probability are primarily found on the cope surfaces of the castings. This is due to the buoyancy of reoxidation inclusions in steel castings, which causes the larger inclusions to rise up to the casting surface. In the spindle casting in Fig. 10b, the inclusions concentrate on the lower half of the concave surface leading into the inner diameter of the spindle. However, this is essentially a cope surface, because there

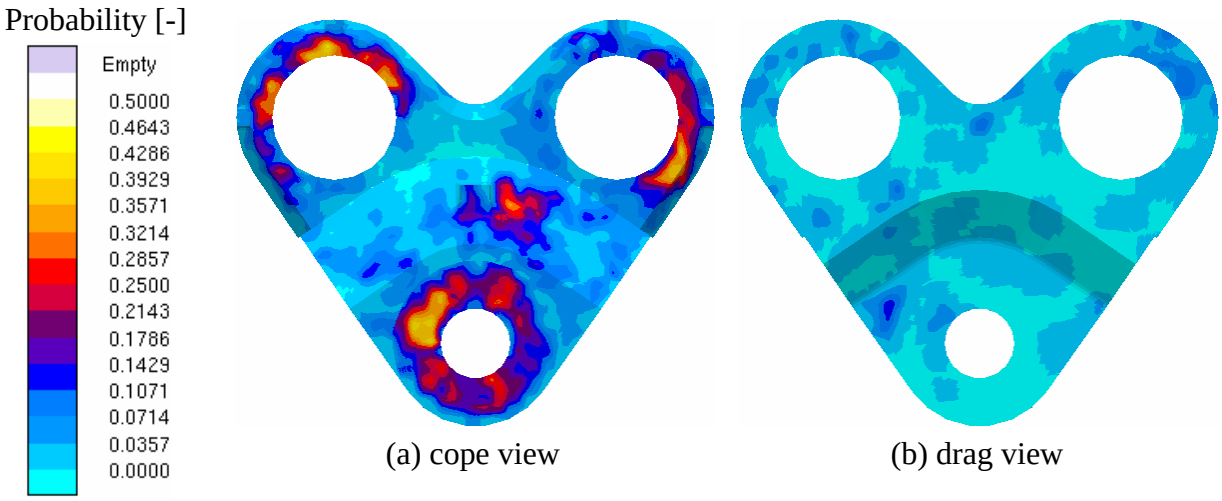

Figure 9. Final measured inclusion probability distribution for the bracket casting: (a) cope surface, and (b) drag surface.

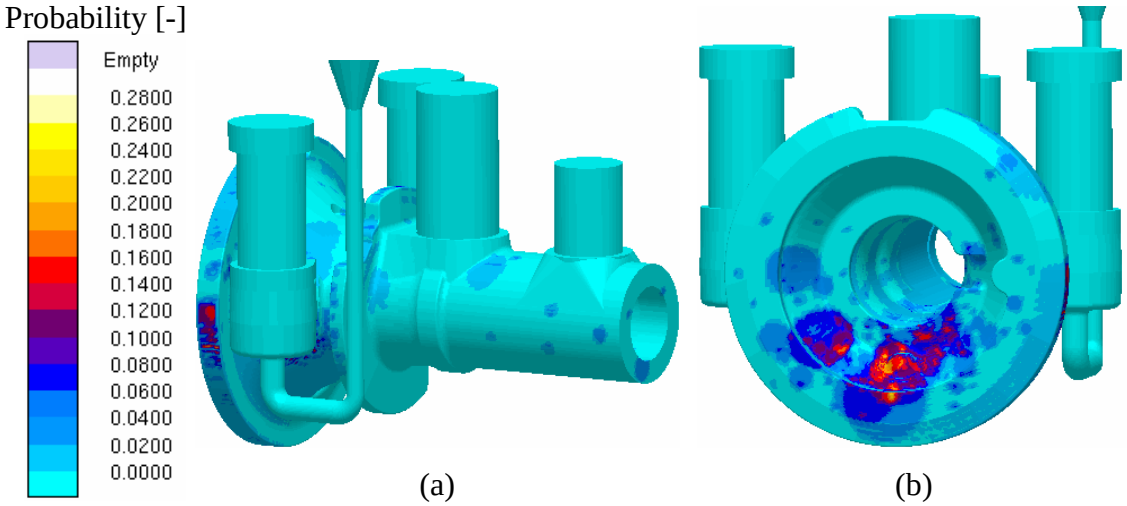

Figure 10. Two views of the final measured inclusion probability distribution for the spindle casting.

is a core in the spindle that acts as an upper mold/metal interface surface, and inclusions rise to the casting surface there as well.

4. Comparing Simulated and Measured Results – Bracket

A filling simulation using the present inclusion model was performed first for the bracket casting. The pouring temperature, time and head height used for the simulation were the average of the values recorded for all 28 bracket castings. A uniform (i.e., $\Delta x = \Delta y = \Delta z = \text{constant}$) 4 mm computational grid was used for the bracket simulation, which produces 1,177,000 computational cells in the mold cavity (i.e., metal cells). The simulation results presented in this section were generated using the base case inclusion simulation parameters, which are $\lambda_{inc} = 0.25$ mm and $L_{sp} = \Delta x =$ 4 mm. The selection of these parameters, as well as the grid size, will be discussed in the parametric studies provided in the next section.

4.1 Simulated Inclusions

The inclusions resulting from the bracket simulation are shown at different times during filling in Fig. 11. The scale in this figure indicates the inclusion diameter. For visualization purposes, inclusions are shown twice their actual size. Inclusions mark the metal free surface as it flows into the bracket via the ingate, around the top ring, down the bracket's inclined slope, around the two bottom rings, and then back up the inclined slope to complete the filling of the bracket. As filling proceeds, inclusion sizes are seen to increase as inclusions grow and agglomerate.

Fig. 12 shows a closer view of the inclusions after the metal fills the two bottom rings and begins to move back up the inclined slope. The scale for Fig. 12 is the same as shown in Fig. 11. The wave of metal beginning up the inclined slope is marked by a large concentration of inclusions, which are circled in Fig. 12 (the arrows indicate the direction the wave is moving). The larger inclusions in the circle were generated when the metal streams that went around the two lower rings met between these rings as the metal began to flow back up the casting. This phenomenon is commonly seen in inclusion simulation results; when metal free surfaces meet, the free surface inclusions at the wave fronts tend to agglomerate and create larger inclusions.

Finally, a cope surface view of the inclusion distribution at the end of filling is shown in Fig. 13a. In this view, inclusions smaller than 0.25 mm are not shown, in order to more clearly see the

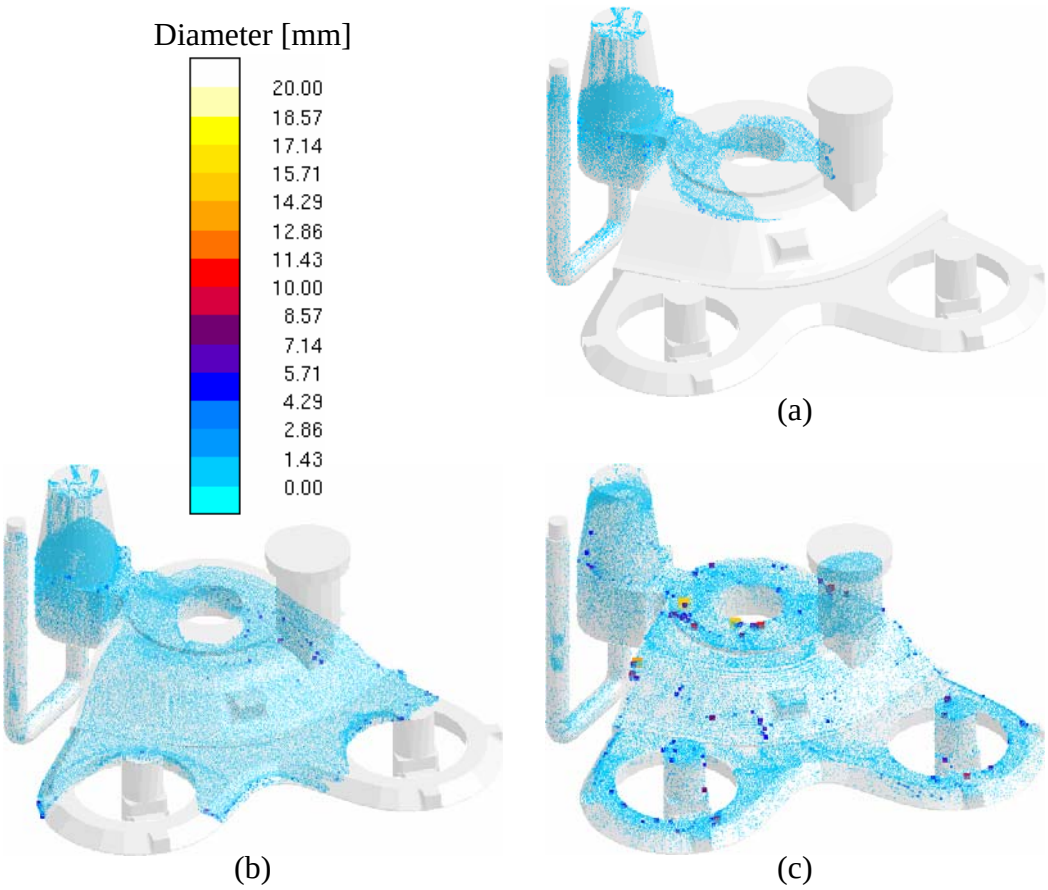

Figure 11. Base case simulation results for the bracket, showing inclusions generated during the filling sequence for the bracket casting. The scale indicates the diameter of each inclusion. Inclusions are displayed at twice their actual size.

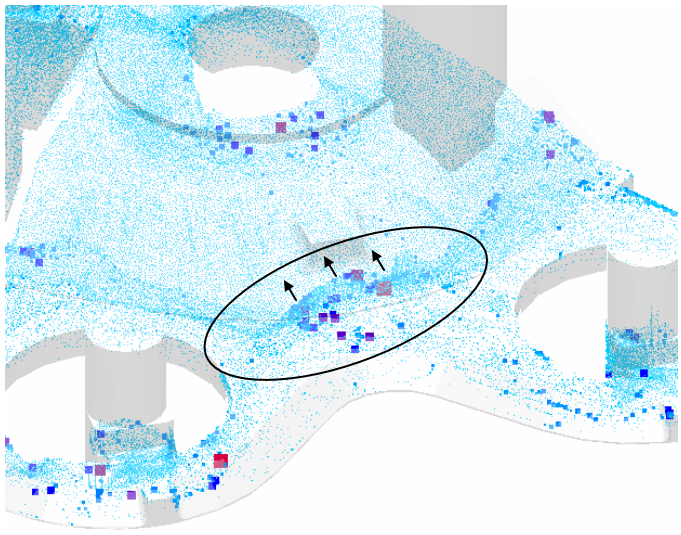

Figure 12. Base case simulation results for the bracket, showing a wave of inclusions moving up the sloped bracket surface. Inclusions are displayed at twice their actual size.

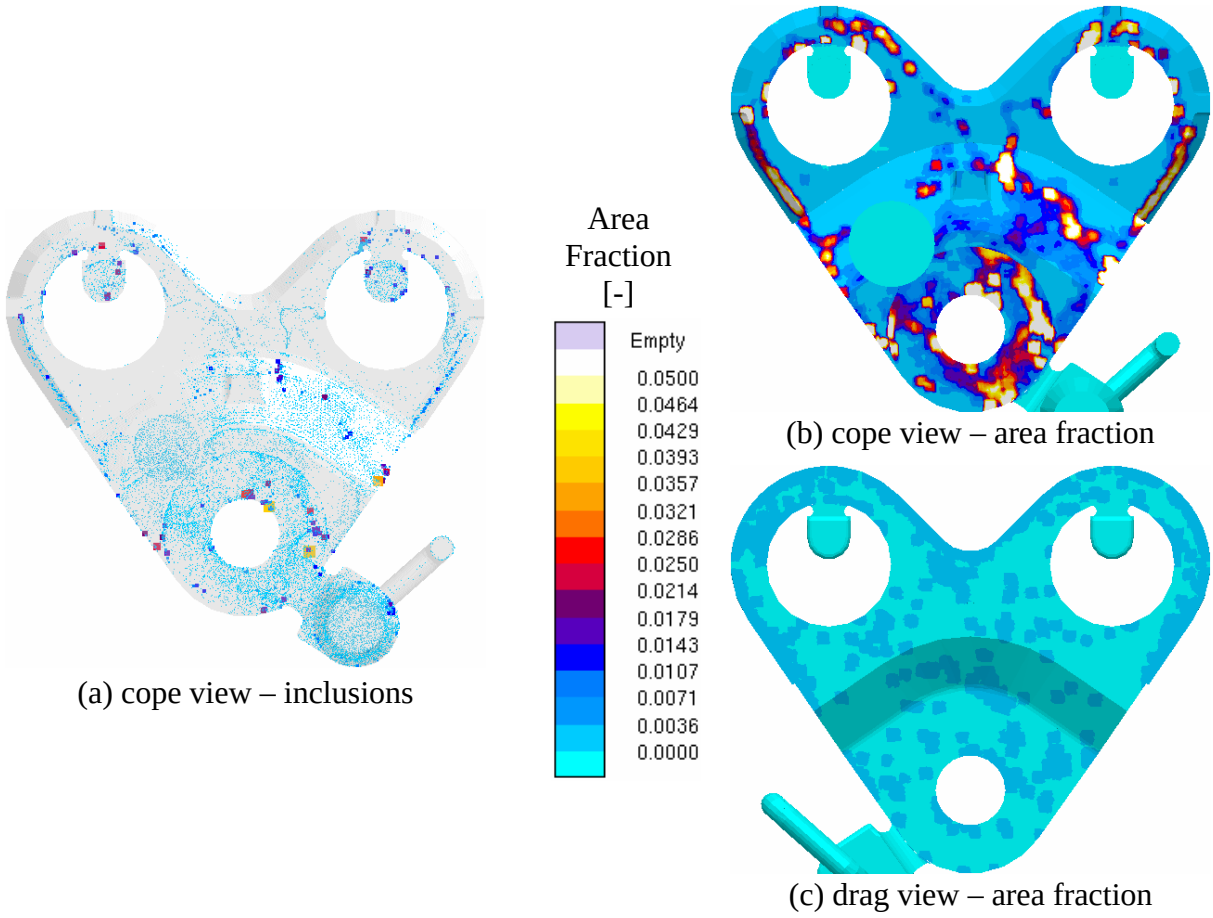

(a) cope view – inclusions

(b) cope view – area fraction

(c) drag view – area fraction

Figure 13. Base case simulation results for the bracket, showing (a) cope surface view of final inclusion distribution at the end of filling (scale given in Fig. 11), (b) cope surface view of resulting surface inclusion area fraction distribution, and (c) drag surface view of inclusion area fraction distribution.

significant inclusions. For this final inclusion distribution, the maximum inclusion diameter is 15.6 mm, while the average diameter is 0.852 mm. The final number of inclusions is 77,400, which is an inclusion number density of 1.03×10^{6} m^{-3}. The inclusion volume fraction is 333 ppm. Comparable values were found for the lever arm and spindle as well. These values all indicate that the simulations track a reasonable number of the larger inclusions that occur, and that the sizes and volume of these inclusions are reasonable as well.

4.2 Converting Inclusion Distribution to Area Fraction Distribution

In order to qualitatively compare the final simulated inclusion distribution to the measured inclusion probability result for the bracket (shown in Fig. 9), surface inclusion area fraction plots were generated based on the final inclusion locations at the end of filling. This area fraction was

determined by computing, for each computational cell at the casting free surface, the total cross-sectional area of the inclusions in that control volume divided by the casting surface area for that cell. In addition, moving-average smoothing was performed on the area fraction results with a stencil size of ~2.54 cm (~1 in.), in order to match the minimum resolution of the measured results shown in the previous section.

To illustrate the conversion from final inclusion distribution to inclusion area fraction, Fig. 13b shows the inclusion area fraction distribution corresponding to the final inclusion distribution shown in Fig. 13a. For the purpose of comparison with measurements, the area fraction result on the drag surface is provided in Fig. 13c. The magnitude of the values on the area fraction scale are relatively arbitrary, since changing the size of the region over which the area fraction is evaluated will change the magnitude, as will changing the stencil size for the moving average smoothing. Values are really only important relative to each other: values near zero indicate regions with no inclusions or only a few small inclusions, and values at or above the maximum on the scale indicate regions with either large inclusions or large numbers of smaller inclusions. The inclusion area fraction is only calculated on the casting surface (i.e., not on the surfaces of the risers and gating, which are shown to orient the reader to the casting). As a result, when the risers and/or gating are shown in area fraction plots such as Figs. 13b and 13c, they appear to have an area fraction of zero.

4.3 Comparing Simulated and Measured Results

The bracket inclusion area fraction distributions shown in Fig. 13 are compared with the measured inclusion probability distributions shown in Fig. 9. No attempt should be made to compare these figures quantitatively; aside from the relatively arbitrary nature of the area fraction values mentioned above, this is a comparison between the amount of inclusions predicted by a single filling simulation and the probability of inclusions being present, based on 28 castings. However, these results can be qualitatively compared by comparing high and low regions of inclusion area fraction and inclusion probability.

Considering the cope surface probability distribution in Fig. 9a, notice that there are four regions that have a relatively high probability of inclusions: around the ring near the ingate (bottom ring in this figure), around parts of the two rings away from the ingate (top rings), and to the right of the boss in the middle of the inclined surface between the top and bottom rings. The simulated inclusion area fraction distribution on the cope surface (Fig. 13b) shows good

agreement in these areas: there are significant indications around the bottom ring, as well as around the parts of the two top rings where the inclusion probability is high in Fig. 9a. There are also significant area fraction indications near the region of high probability on the inclined surface, although the area fraction indications are somewhat more dispersed. Also noteworthy is the agreement in several areas with a low inclusion probability in Fig. 9a: the area below both top rings and the bulk of the inclined surface have low inclusion probabilities, and the area fraction indications seen in Fig. 13b in these regions are correspondingly small. There are a couple of low probability regions in Fig. 9a where inclusions are predicted in Fig. 13b, such as on the right and left edges of the inclined surface, but overall the agreement is very satisfactory. Comparison of the drag surface probability distribution (Fig. 9b) and area fraction distribution (Fig. 13c) also indicates good agreement, with far fewer indications than on the cope surface, and the bulk of the inclusions that are seen on the drag surface concentrated around the two upper rings. The drag surface is much cleaner than the cope due to buoyancy effects, which are taken into account in the model.

5. Parametric Studies – Bracket

In addition to the base case simulation utilized in the previous section, parametric studies were also performed for the bracket casting, in order to determine the effect of model parameters (namely, the slip coefficient, λ_{inc}, and the agglomeration length, L_{sp}) and the computational grid on the final inclusion area fraction distributions. The results of these parametric studies are presented in this section.

5.1 Slip Coefficient Study

The first parametric study performed for the bracket investigates the effect of the slip coefficient, λ_{inc}, defined in equation (6). For the slip coefficient simulations, base case parameters were used for the grid size ($\Delta x =$ 4 mm, uniform grid) and the agglomeration length (i.e., $L_{sp} = \Delta x =$ 4 mm). Cope surface inclusion area fraction distributions are provided in Fig. 14 for $\lambda_{inc} =$ 0 (no slip) and $\lambda_{inc} \to \infty$ (full slip). The scale for Fig. 14 is given in Fig. 13. Simulations were performed at several other partial slip lengths between zero and infinity, but the base case ($\lambda_{inc} =$ 0.25 mm) result shown in Fig. 13b was in the best agreement with the

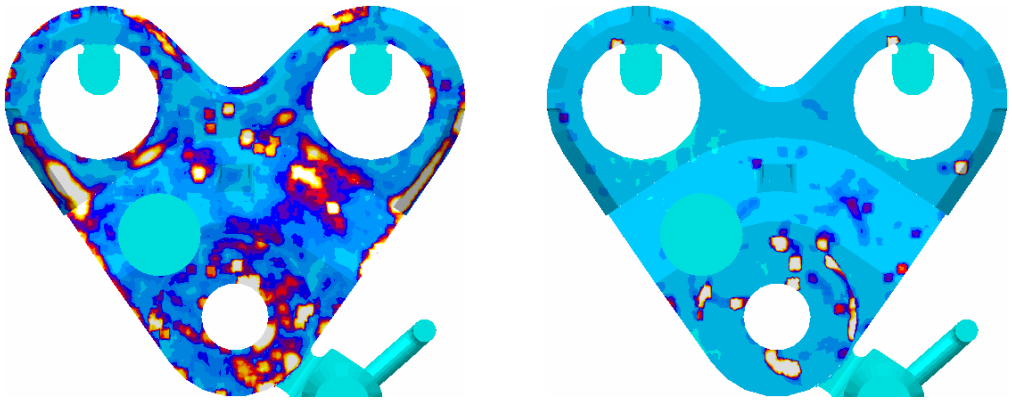

(a) $\lambda_{inc} = 0$ (no slip) (b) $\lambda_{inc} \to \infty$ (full slip)

Figure 14. Simulated inclusion area fraction distribution on the bracket cope surface using base case simulation conditions except for the slip coefficient: (a) $\lambda_{inc} = 0$ (no slip), (b) $\lambda_{inc} \to \infty$ (full slip).

measured probability distribution given in Fig. 9a. The most obvious conclusion that can be drawn from Fig. 14 is that the full slip result shown in Fig. 14b is in relatively poor agreement with the measured result. Inclusions slide too readily away from the two top rings, leaving those rings almost inclusion-free. There are a few moderate area fraction indications on the inclined surface between the two top rings and the bottom ring, and there are some severe indications around the bottom ring, both of which qualitatively agree with the measurements. However, in general there are far fewer indications in Fig. 14b than in the measured result in Fig. 9a. The area fraction results for no slip (Fig. 14a) and partial slip (Fig. 13b) are relatively similar. Both have significant indications around all three rings, as well as on the right side of the inclined surface between the top and bottom rings; these trends agree with the measured probability distribution. However, the partial slip result agrees with the measured distribution somewhat better than the no slip result in two respects. First, the indications around the top rings are too close to the edge of the casting in the no slip case, but move in more toward the inside of those rings in the partial slip case. Second, the partial slip case has regions below both of the top rings that are relatively inclusion-free, in agreement with the measured distribution. By contrast, the no slip case has significant indications in these regions below the top rings. As a result of this comparison, although the no slip and the partial slip results both give reasonable agreement with the measured result, the partial slip result gives better agreement.

5.2 Computational Grid Size Study

Next, the effect of computational grid size is investigated. For this parametric study, base case parameters were used for the slip coefficient (λ_{inc} = 0.25 mm) and the agglomeration length (L_{sp} = 4 mm). The results for the base case 4 mm grid are compared to results from a 7 mm uniform grid. The cope surface inclusion area fraction distribution resulting from the 7 mm grid is provided in Fig. 15. The scale for Fig. 15 is given in Fig. 13. For the bracket casting, a 7 mm uniform grid creates 216,000 metal cells, which is over five times fewer metal cells than in the base case grid. The simulation results using a 7 mm grid (Fig. 15) and the base case grid (Fig. 13b) are similar, in that they both show significant area fraction indications around all three rings and they both have relatively inclusion-free regions below the two top rings. In these respects, both results are in good agreement with the measured distribution in Fig. 9a. The primary difference is that the base case result shows significant indications on the inclined surface between the top rings and the bottom ring (in agreement with the measured distribution), while Fig. 15 shows few indications on that surface. The inclusions that gather on the inclined surface in Fig. 13b are also present in Fig. 15; they are represented by the cluster of indications between the two top rings. In the base case simulation, these inclusions move past the region between the top rings and settle on the inclined surface. However, in the 7 mm grid simulation, these inclusions remain between the two top rings. This may be due to differences in the filling simulations. Changing the grid changes the flow simulation (due to changes in spatial resolution, time step, etc.). This leads to differences in the way the free surface evolves during filling, as

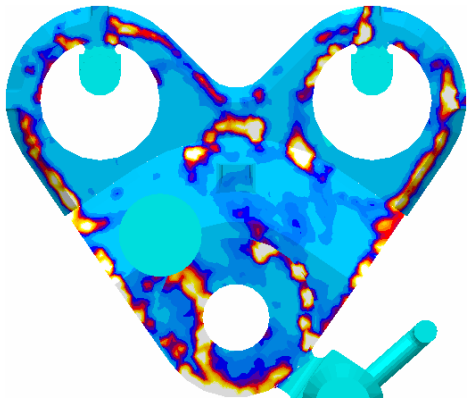

Figure 15. Simulated inclusion area fraction distribution on the bracket cope surface using base case simulation conditions except for the numerical grid, which is 7 x 7 x 7 mm.

well as differences in exactly when and how often inclusion computations are performed during the simulation, both of which alter the final inclusion distribution.

5.3 Agglomeration Length Study

The final parametric study considers the effect of the agglomeration length on the final inclusion distribution. The base case grid size (4 mm) and slip coefficient (λ_{inc} = 0.25 mm) were used for all simulations in this study. The cope surface area fraction distribution for the base case agglomeration length (L_{sp} = 4 mm), shown in Fig. 13b, is compared to simulation results with agglomeration lengths of 2 mm (Fig. 16a) and 1 mm (Fig. 16b). The scale for Fig. 16 is given in Fig. 13. Values of L_{sp} larger than the grid size are not investigated because the agglomeration spacing is kept equal to the inclusion generation spacing, and the generation spacing is limited to the grid size or smaller in order to ensure that there is at least one inclusion per computational melt free surface cell. This is necessary to conserve oxide volume, because the apportioning of new oxide to inclusions in the growth model is done in each computational cell.

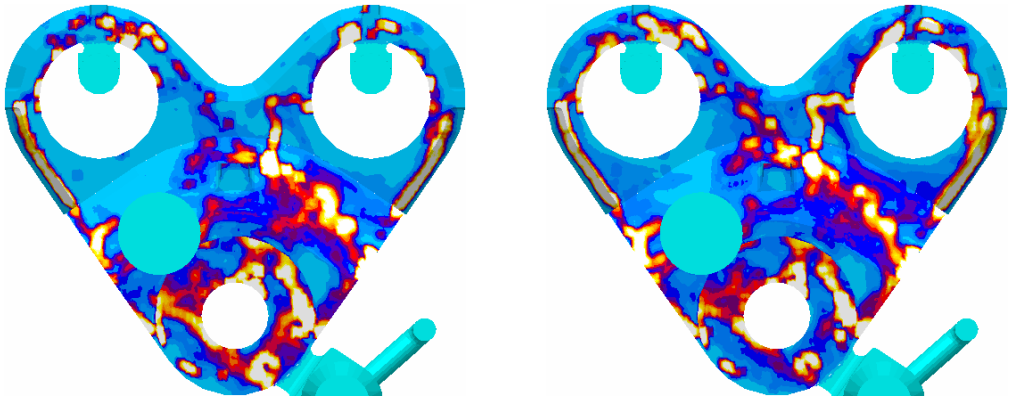

(a) L_{sp} = 2 mm (b) L_{sp} = 1 mm

Figure 16. Simulated inclusion area fraction distribution on the bracket cope surface using base case simulation conditions except for the agglomeration length: (a) L_{sp} = 2 mm, (b) L_{sp} = 1 mm.

Comparing these figures, it is evident that changing the agglomeration length does not significantly change the final inclusion locations. Decreasing the agglomeration length is seen to almost uniformly increase the inclusion area fraction magnitude. In other words, different area fraction scales could be chosen for Figs. 16a and 16b that would make these results look quite

similar to Fig. 13b. Since the values on the area fraction scale are more or less arbitrary, and only relative intensities are important, this implies that the agglomeration length has little effect on the inclusion area fraction distribution. It does, however, have a profound impact on the final number of inclusions in the simulation: 77,400 inclusions resulted from the simulation with $L_{sp} = 4$ mm, while 894,000 inclusions resulted from the simulation with $L_{sp} = 1$ mm. Thus, it is recommended to use an agglomeration length equal to the grid spacing.

6. Comparing Simulated and Measured Results – Lever Arm

Next, a simulation was performed for the lever arm casting (see Fig. 7). Again, the pouring temperature, time and head height used for the simulation were the average of the values recorded for all 29 lever arm castings. A uniform 10 mm computational grid was used for the simulation, which produces 139,000 metal cells. The simulation utilized the base case inclusion simulation parameters, $\lambda_{inc} = 0.25$ mm and $L_{sp} = \Delta x = 10$ mm.

Regarding the lever arm results, note from Fig. 7 that two levers are cast in the same mold: lever 1 and lever 2. The 29 lever arm castings utilized in this study were not denoted as being cast in the lever 1 or lever 2 position, so the measured probability distribution shown in Figs. 8b and 8c is an average of the two levers. Because of this, it was necessary to construct for the simulation results a similar average area fraction distribution. The cope view of the inclusion area fraction distribution at the end of filling for the base case simulation is shown in Fig. 17a for lever 1 and in Fig. 17b for lever 2. Note that the inclusion distributions in these two levers have similarities, but also some differences. The differences are due to asymmetric flow patterns in the two levers during filling. The average area fraction result was constructed by averaging the lever 1 and lever 2 area fraction distributions, which resulted in the average distribution shown in Fig. 17c.

Cope surface views of the measured average inclusion probability and the simulated average inclusion area fraction distributions are compared in Figs. 18a and 18b, respectively. The scale for Fig. 18a is given in Fig. 8, and the scale for Fig. 18b is given in Fig. 17. There is relatively good agreement between the measured probability distribution and the simulated area fraction distribution. The largest indications are seen on the long edges of the lever arm (both ingate side and opposite side) in both the measurement and the simulation results, with far fewer indications

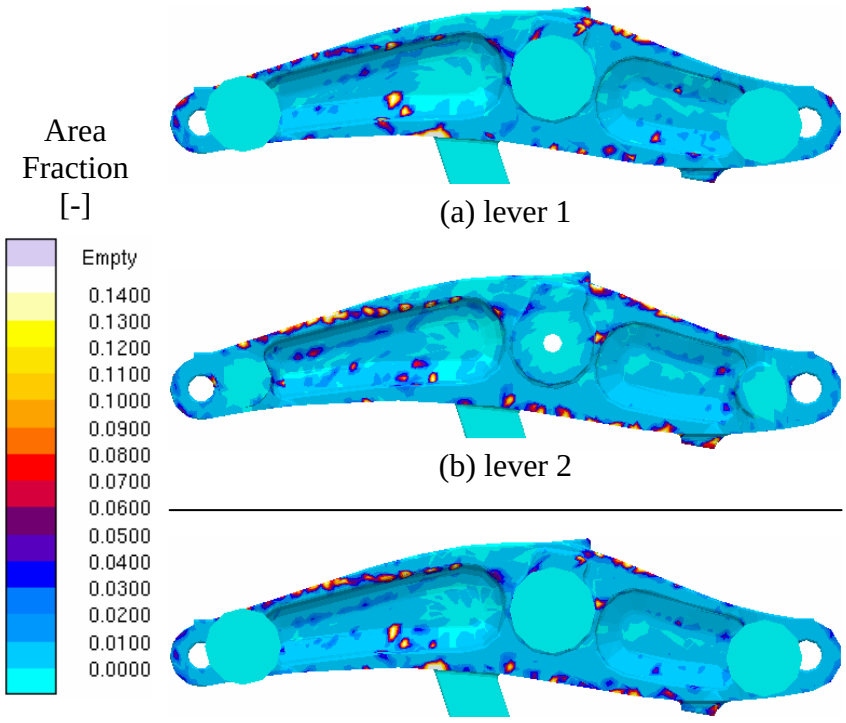

(a) lever 1

(b) lever 2

(c) average of levers 1 and 2

Figure 17. Cope surface views of the base case simulation inclusion area fractions for (a) lever 1, (b) lever 2, and (c) the average of levers 1 and 2.

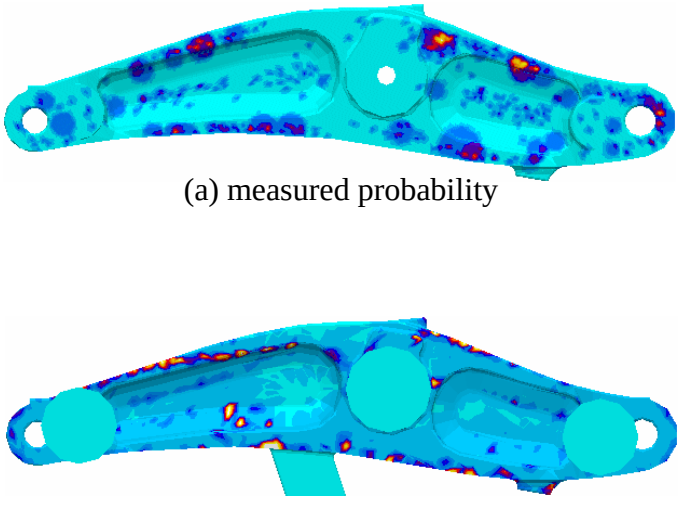

(a) measured probability

(b) simulated area fraction

Figure 18. (a) Measured probability of inclusions being present on the lever arm cope surface, compared to (b) base case simulation inclusion area fractions.

in the webbing between the edges. Fig. 18a indicates that the highest measured inclusion probability regions are located on the right half of the top edge. The simulated area fraction

distribution in Fig. 18b also contains high area fractions in that region, although the high area fractions are closer to the edge than in the measured result.

Finally, Fig. 19 shows the simulated average area fraction distribution on the lever arm, using the same views shown for the corresponding probability results in Fig. 8. The scale for Fig. 19 is given in Fig. 17. Comparing Fig. 19b to Fig. 8c, it is seen that the drag surfaces are relatively clean in both measurement and prediction, again due to the buoyancy of reoxidation inclusions in steel.

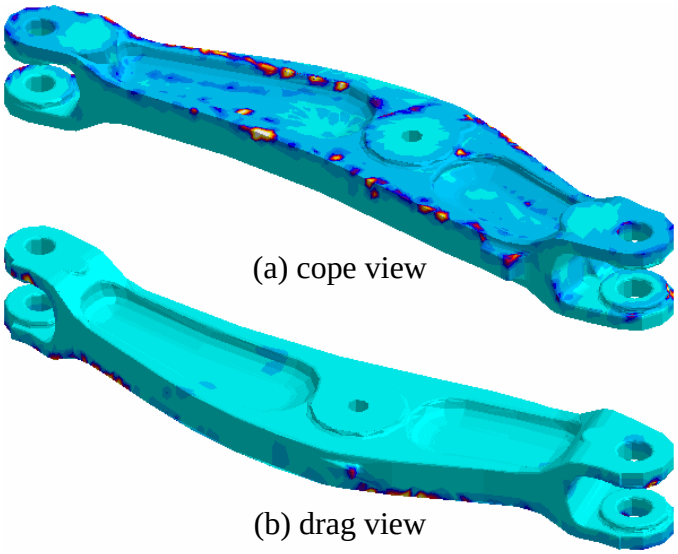

(a) cope view

(b) drag view

Figure 19. Lever arm base case simulation results, showing (a) cope surface view, and (b) drag surface view of average inclusion area fraction distribution.

7. Comparing Simulated and Measured Results – Spindle

The final part considered in the present study is a spindle, shown schematically in Fig. 6. The spindle was simulated, again using average pouring temperature, time and head height values from the 30 spindle castings, on a uniform 10 mm computational grid, which produces 477,000 metal cells. The base case inclusion simulation parameters ($\lambda_{inc} = 0.25$ mm and $L_{sp} = \Delta x =$ 10 mm) were also used.

The measured inclusion probability distribution (based on 30 castings) for this part is shown in Fig. 10. The inclusion area fraction distribution at the end of filling for the base case simulation of the spindle is shown in Fig. 20. In comparing simulated area fractions with

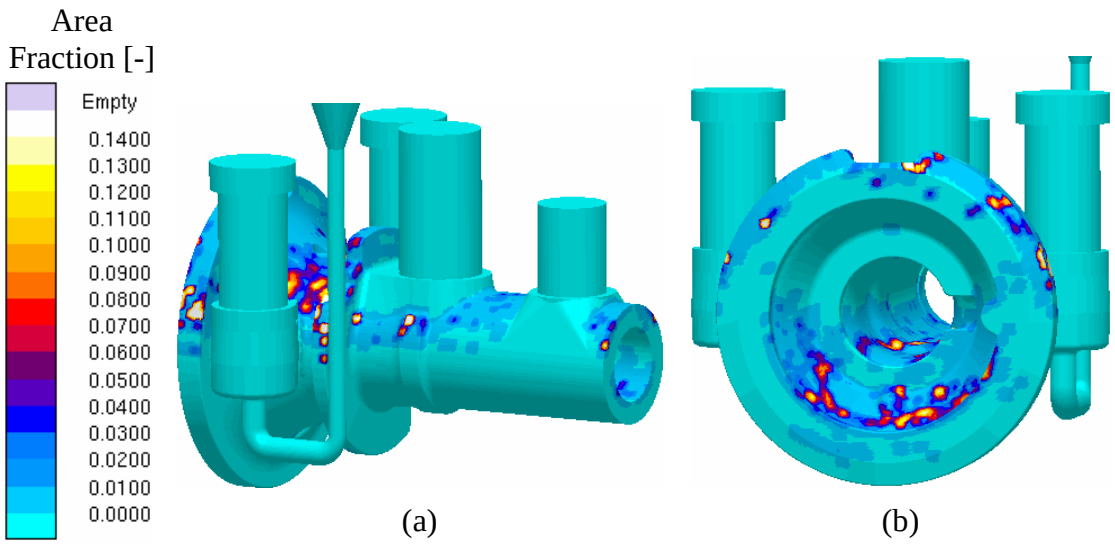

Figure 20. Two views of the inclusion area fraction distribution resulting from the base case simulation of the spindle casting.

measured inclusion probabilities, it is important to note that the exterior surfaces of all of the spindle castings were machined before inclusion measurements were performed. Thus, surface inclusions may have been removed, and sub-surface inclusions may have been uncovered. The "bell" region of the casting, which is the concave region leading from the front flange to the inside diameter of the spindle (see Fig. 20b), was not machined, and therefore is the primary focus of this discussion.

Comparing measured and simulated inclusion results in this region (Figs. 10b and 20b), one sees reasonable agreement between simulation and measurements. The highest concentration of inclusions is in the lower half of the bell surface, while the upper half of this surface is relatively free of inclusions. As noted earlier, the lower half of the bell surface is essentially a cope surface, since the core forms an upper boundary in this region. Inclusions rise in the melt until they reach the melt/core surface, and then they slide along this surface, influenced by the local flow patterns and buoyancy. The area fraction result in Fig. 20b also shows some significant inclusions on the top of the front flange; these inclusions are the result of larger inclusions rising due to buoyancy. Such indications are not evident in the measurements, but this surface was machined.

The measured and simulated distributions for the side of the spindle are shown in Figs. 10a and 20a, respectively. The only prominent feature in the measured distribution shown in Fig. 10a is the inclusion indication on the side of the front flange, and the simulated distribution (Fig. 20a)

also shows a strong area fraction indication in this region. The remainder of Fig. 10a is largely inclusion-free, which is likely the result of machining. Fig. 20a shows several indications on the body of the spindle. Notice that they are on the cope surface; this is again the result of buoyancy.

Finally, it should be noted that parametric studies such as those shown in Section 5 were also performed for the lever arm and spindle castings. The results of the parametric studies for the lever arm and the spindle produced the same trends as seen for the bracket, and are therefore not shown here. For all three parts, the inclusion area fraction distributions resulting from the base case simulation conditions produced the best agreement with the measured probability distributions.

8. Conclusions

A model for simulating the growth and movement of reoxidation inclusions during pouring of C&LA steel sand castings has been developed that predicts the distribution of the inclusions on the casting surface. The model is validated by comparing the simulation results to inclusion measurements made on three production steel casting parts. Good agreement is seen between simulated and measured inclusion distributions. In addition, the simulations also produce reasonable inclusion sizes and total inclusion volumes. Parametric studies are performed to investigate the sensitivity of the predictions to model parameters. These studies indicate the following: (1) an inclusion motion model allowing partial slip of inclusions in contact with mold/core surfaces gives better agreement with measurements than does a model with no slip or full slip; (2) the grid size affects the final inclusion distribution to some degree—overall reasonable agreement with the measured distribution is maintained, but noticeable differences are evident; and (3) the agglomeration length, which is used to limit the number of inclusions in a simulation to a reasonable value, does not have a significant effect on the final inclusion distribution.

Acknowledgements

This work was supported by the Iowa Energy Center under grant number 06-01. The authors would like to thank Harrison Steel Castings Company and MAGMA GmbH for their generous support through the donation of software, time and information. The authors would also like to thank Dr. Frank Peters and his research group at Iowa State University for their inclusion measurement data for the bracket casting.

References

1. J.A Griffin and C.E. Bates: 'Ladle Treating, Pouring and Gating for the Production of Clean Steel Castings,' Steel Founders' Society of America (SFSA) Research Report No. 104, Crystal Lake, Illinois, 1991.
2. L. Wang and C. Beckermann: *Metall. Mater. Trans. B*, 2006, **37B**, 571-588.
3. A.J. Melendez, K.D. Carlson, and C. Beckermann: Proc. 61st SFSA Technical and Operating Conference, Chicago, Illinois, December 2007.
4. W.E. Ranz and W.R. Marshall, Jr.: *Chem. Eng. Prog.*, 1952, **48(4)**, 141–146.
5. L. Zhang and B.G. Thomas: *ISIJ Int.*, 2003, **43(3)**, 271-291.